

InGaP $\chi^{(2)}$ integrated photonics platform for broadband, ultra-efficient nonlinear conversion and entangled photon generation

Joshua Akin,^{1,2,*} Yunlei Zhao,^{1,2,*} Yuvraj Misra,^{1,2} A. K. M. Naziul Haque,^{1,2} and Kejie Fang^{1,2,†}

¹*Holonyak Micro and Nanotechnology Laboratory and Department of Electrical and Computer Engineering, University of Illinois at Urbana-Champaign, Urbana, IL 61801 USA*

²*Illinois Quantum Information Science and Technology Center, University of Illinois at Urbana-Champaign, Urbana, IL 61801 USA*

Nonlinear optics plays an important role in many areas of science and technology. The advance of nonlinear optics is empowered by the discovery and utilization of materials with growing optical nonlinearity. Here we demonstrate an indium gallium phosphide (InGaP) integrated photonics platform for broadband, ultra-efficient second-order nonlinear optics. The InGaP nanophotonic waveguide enables second-harmonic generation with a normalized efficiency of 128,000%/W/cm² at 1.55 μm pump wavelength, nearly two orders of magnitude higher than the state of the art in the telecommunication C band. Further, we realize an ultra-bright, broadband time-energy entangled photon source with a pair generation rate of 97 GHz/mW and a bandwidth of 115 nm centered at the telecommunication C band. The InGaP entangled photon source shows high coincidence-to-accidental counts ratio CAR > 10⁴ and two-photon interference visibility > 98%. The InGaP second-order nonlinear photonics platform will have wide-ranging implications for non-classical light generation, optical signal processing, and quantum networking.

Introduction

The development of nonlinear optics is empowered by the invention of nonlinear materials, from bulk nonlinear crystals and silica fibers to more recent wafer-scale thin-film materials. Over the past decades, the application of materials with increasing nonlinearities, combined with the advance of light-confining nanophotonic structures, has resulted in a remarkable enhancement in nonlinear optical efficiencies. For example, the second-harmonic generation has advanced from the initial demonstration using a quartz crystal with a 10⁻⁹%/W efficiency [1] to the record of 10⁵ – 10⁶%/W achieved in thin-film nanophotonic resonators nowadays [2, 3].

Second-order ($\chi^{(2)}$) optical nonlinearity, as the dominant optical nonlinearity, enables a variety of nonlinear optical processes with high efficiencies and low noises, including generation of entangled photons [4] and squeezed light [5], parametric optical amplification [6], and coherent wavelength conversion [7]. Fig. 1a displays the second-order susceptibility and cutoff wavelength of a selection of $\chi^{(2)}$ materials that are available in thin-film platforms. Among them, III-V semiconductors, including GaAs and Al_xGa_{1-x}As, are notable for the very high second-order susceptibility, leading to a long history of study for nonlinear optics [8]. The versatile III-V photonics platform enables heteroepitaxial integration of pump lasers and photodetectors, which is unique compared to other platforms. However, one drawback of these III-V semiconductors is the optical losses at short wavelengths. For example, GaAs has a narrow bandgap corresponding to a cutoff wavelength of 872 nm. While Al_xGa_{1-x}As exhibits a wider bandgap, its second-order susceptibility

decreases drastically with the increasing aluminum composition [9]. Moreover, arsenic III-V materials suffer from strong optical absorption at wavelengths less than 800 nm, due to the antibonding As-As surface state that is below the bandgap [10–12]. These facts have limited the use of arsenic III-V materials for efficient second-order nonlinear optics in the important telecommunication C band (1530-1565 nm), where long-haul optical communications conducts, due to the absorption of the corresponding second harmonics.

Indium gallium phosphide (In_{0.5}Ga_{0.5}P, hereafter referred to as InGaP) is another III-V semiconductor material that is lattice-matched with GaAs and thus can be epitaxially grown on the GaAs substrate at the wafer scale. Because of its high electron mobility, direct bandgap, and thermal stability, InGaP has been used for making heterojunction bipolar transistors [13], solar cells [14], photodetectors [15], and LEDs [16]. More recently, thin-film InGaP has been explored for third-order nonlinear optics using its substantial Kerr nonlinearity [17, 18], resulting in demonstrations of frequency combs [19], optical parametric oscillators [20], and entangled photon pairs via four-wave mixing [21].

Besides its notable Kerr nonlinearity, InGaP is particularly appealing for second-order nonlinear optics because of the combination of a substantial second-order susceptibility ($\chi_{xyz}^{(2)} \approx 220$ pm/V [27]) and a sizable bandgap of 1.92 eV (cutoff wavelength 645 nm). For InGaP, the antibonding anion state lies well above the bandgap [11], in contrast to Al_xGa_{1-x}As, which avoids light absorption before the bandgap. InGaP also has a large refractive index (> 3), which facilitates nanophotonic structures with strong light confinement. These properties suggest the potential of InGaP for realizing highly-efficient second-order nonlinear optics, in particular, in the crucial telecommunication C band. Recently, several research groups have embarked on studying second-order nonlin-

* These authors contributed equally to this work.

† kfang3@illinois.edu

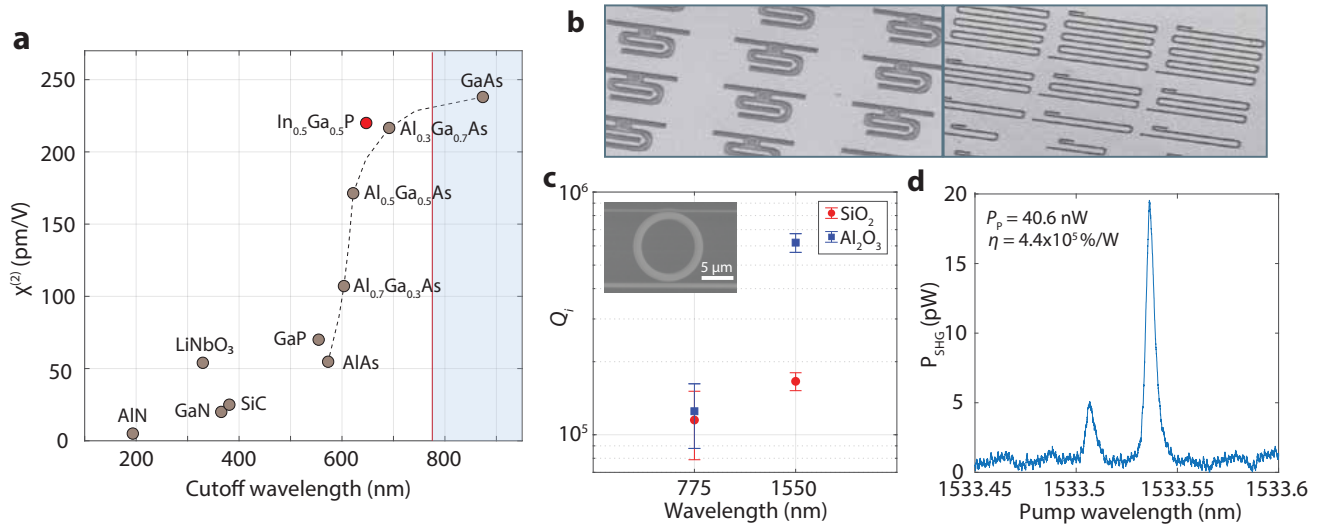


FIG. 1. **a**. Second-order susceptibility and cutoff wavelength of several nonlinear optical thin-film materials. The red line indicates the 775 nm wavelength. Shaded region indicates optical absorption at wavelengths longer than 775 nm. AlN: [22], LiNbO₃: [23], GaN: [24], SiC: [25], GaP: [26], AlGaAs: [9], GaAs: [26], InGaP: [27]. **b**. SEM images of InGaP photonic integrated circuits. **c**. Intrinsic quality factor of the 1550 nm TE₀₀ and 775 nm TM₀₀ resonances of $R = 5 \mu\text{m}$ InGaP microring resonators (inset) with SiO₂ and Al₂O₃ claddings. **d**. Second-harmonic generation in a $R = 5 \mu\text{m}$ phase-matched InGaP microring resonator with Al₂O₃ cladding. On-chip pump power is 40.6 nW and the peak SHG efficiency is 440,000 %/W.

ear optics using thin-film InGaP [3, 28, 29]. Despite demonstrating a record nonlinearity-to-loss ratio in InGaP microring resonators [3], most demonstrations thus far are still limited by considerable optical losses and imperfect phase matching condition. Moreover, InGaP microcavities demonstrated in Ref. [3] are unsuitable for applications that demand broadband operation and high optical powers. As a result, realizing a broadband, low-loss, ultra-efficient second-order nonlinear photonics platform based on InGaP remains elusive.

Here, through the optimization of optical losses and phase-matching condition for InGaP nanophotonic waveguides across an octave wavelength span, we demonstrate a broadband, ultra-efficient InGaP second-order nonlinear photonics platform in the telecommunication band. The demonstrated second-harmonic generation with a normalized efficiency of 128,000%/W/cm² in the telecommunication C band is nearly two orders of magnitude more efficient than the state of the art [30, 31]. Using the InGaP nanophotonic waveguide, we demonstrate an ultra-bright time-energy entangled photon source with a pair generation rate of 97 GHz/mW and a bandwidth of 115 nm (14.4 THz) centered at the telecommunication C band. The broadband, ultra-efficient InGaP nanophotonics platform will enable a wide range of nonlinear optical processes and applications with unprecedented performances.

Results

In this study, 110 nm thick InGaP is epitaxially grown on the GaAs substrate (0 degree off-cut toward [110]) using metal-organic chemical vapor deposition (T=545 C, V/III=280, with precursors including trimethylindium,

trimethylgallium, and PH₃). The root-mean-square surface roughness of the InGaP thin film is measured to be about 0.3 nm, which is close to the native surface roughness of the GaAs substrate. To fabricate InGaP photonic integrated circuits, bonding of InGaP thin film to low-index substrates have been demonstrated before [29, 35]. Here we adopted a transfer-free approach to fabricate InGaP photonic integrated circuits with low-index oxide top claddings (Methods) [3]. Fig. 1b shows the scanning electron microscopy (SEM) images of fabricated InGaP photonic integrated circuits, including microring resonators and waveguides.

We studied the optical loss of InGaP nanophotonic devices in both 1550 nm and 775 nm wavelength bands with two different oxide claddings, SiO₂ and Al₂O₃, deposited via atomic layer deposition. The optical loss is characterized using the intrinsic quality factor ($Q_i \equiv \frac{\omega}{\kappa_i}$) of InGaP microring resonators. The microring resonator couples with both 1550 nm and 775 nm wavelength-band waveguides, which enable measurement of the transmission spectrum of the device [3]. Q_i is then inferred from the fitting of the resonance spectrum. Fig. 1c shows the measured Q_i of the 1550 nm band fundamental transverse-electric (TE₀₀) resonance and the 775 nm band fundamental transverse-magnetic (TM₀₀) resonance of microring resonators with 5 μm radius and 1 μm width. The average value of $Q_{i,1550}$ for microring resonators with Al₂O₃ cladding is about 6×10^5 , over three times higher than that with SiO₂ cladding. $Q_{i,775}$ is $1 - 2 \times 10^5$ and shows slight improvement with Al₂O₃ cladding. The increase of the quality factor could be attributed to the surface passivation induced by Al₂O₃ [36]. We also made mi-

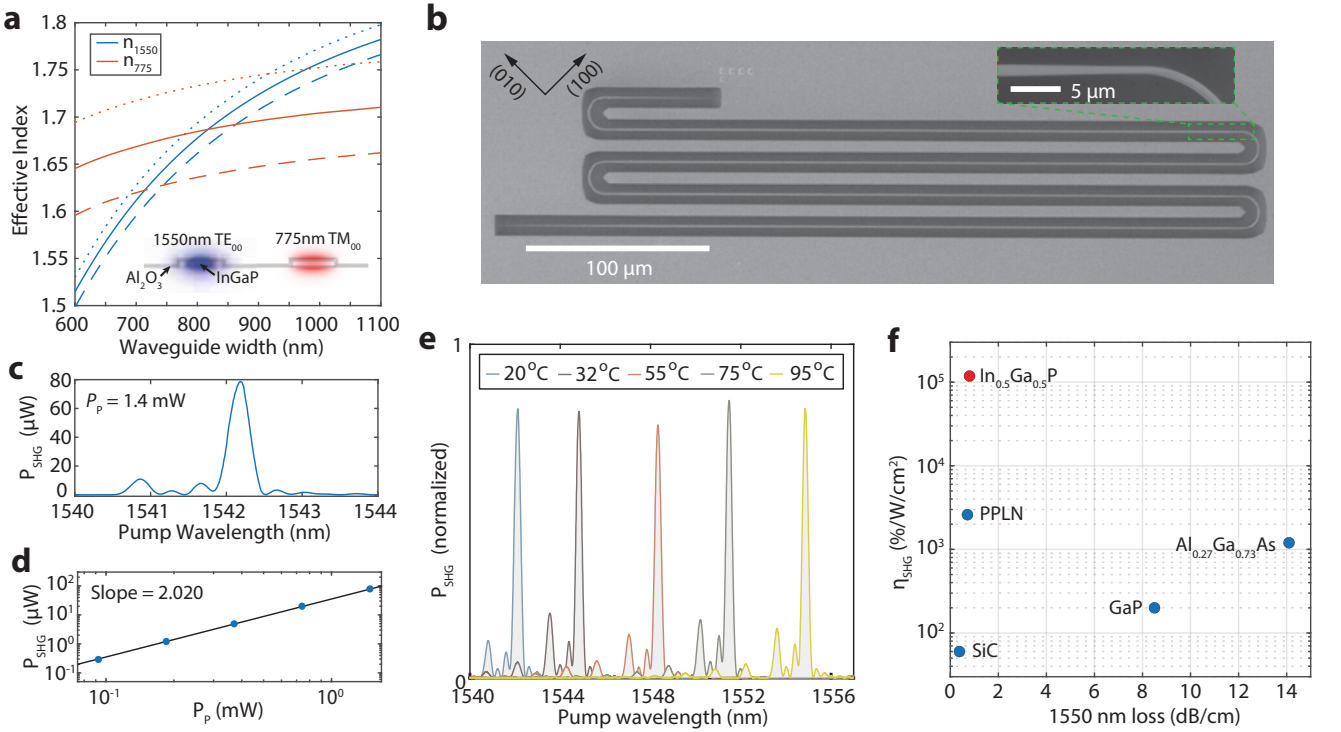


FIG. 2. **a**. Simulated effective mode index of 1550 nm TE_{00} and 775 nm TM_{00} modes of 108 nm (dashed), 110 nm (solid), and 112 nm (dotted) thick InGaP waveguides with 35 nm Al_2O_3 cladding. Inset is a cross section of the waveguide along with the field distribution of the two modes. **b**. SEM images of a fabricated InGaP waveguide device. **c**. Measured SHG spectrum for a 1.6 mm long waveguide device with a pump power of 1.56 mW. **d**. Quadratic relation between the peak SHG power and the pump power. **e**. Temperature tuning of the phase-matching condition. **f**. Normalized SHG efficiency and 1550 nm wavelength band loss of the telecommunication C band waveguide SHG of several thin-film second-order nonlinear photonics platforms. InGaP: this work, PPLN: [30], $Al_{0.27}Ga_{0.73}As$: [32], GaP: [33], SiC: [34].

corings with different sizes and found $Q_{i,1550}$ is peaked around 8×10^5 for larger rings, which is limited by the absorption loss (Supplementary Information (SI)). Leveraging the optimized optical loss, we measured second-harmonic generation (SHG) in a 5- μ m-radius ring with phase-matched 1550 nm band TE_{00} and 775 nm band TM_{00} resonances and realized a resonant nonlinear conversion efficiency $\eta \equiv P_{SHG}/P_p^2 = 440,000\%/W$ (Fig. 1d). This represents a 6-fold enhancement over the previously reported value using the same InGaP microring resonator but with SiO_2 cladding [3].

In contrast to cavities, waveguides can be operated in the broadband regime and circumvent the light extraction issue associated with cavities. Similar to the microring resonator, the InGaP waveguide is designed for phase matching between the 1550 nm band TE_{00} mode a and the 775 nm band TM_{00} mode b , which satisfy $2\omega_a = \omega_b$ and $2k_a = k_b$. Lacking the birefringence in InGaP, phase matching is achieved by dispersion engineering of the InGaP nanophotonic waveguide. By designing the waveguide width, the effective index of the 1550 nm band TE_{00} mode and the 775 nm band TM_{00} mode can be equalized, as shown in Fig. 2a using finite element simulation. For the phase-matched waveguide with length L , the nor-

malized SHG efficiency, $\eta_{SHG} \equiv \frac{P_{SHG}}{P_p^2 L^2}$, can be calculated using [37]

$$\eta_{SHG} = \frac{\omega_a^2}{2n_a^2 n_b \epsilon_0 c^3} \left(\frac{\int d\mathbf{r} \chi_{xyz}^{(2)} \sum_{i \neq j \neq k} E_{bi}^* E_{aj} E_{ak}}{\int d\mathbf{r} |\mathbf{E}_a|^2 \sqrt{\int d\mathbf{r} |\mathbf{E}_b|^2}} \right)^2, \quad (1)$$

where $n_{a(b)}$ is the effective mode index of the fundamental(second)-harmonic mode and the normalization integrals use electric field components perpendicular to the wavevector of the waveguide mode. The SHG efficiency is optimized when the waveguide is aligned along the (110) direction of InGaP, leading to simulated $\eta_{SHG} = 130,000\%/W/cm^2$ for the 1550 nm pump wavelength (SI).

Fig. 2b displays SEM images of a fabricated meander waveguide with a length of 1.6 mm. The waveguide connects to two adiabatically tapered couplers at the end to interface with tapered optical fibers for light transmission. The adiabatic coupler efficiency is approximately 80% and 30% for 1550 nm TE and 775 nm TM polarized light, respectively [3]. The waveguide width is tapered down before entering the 180° turn to avoid mode

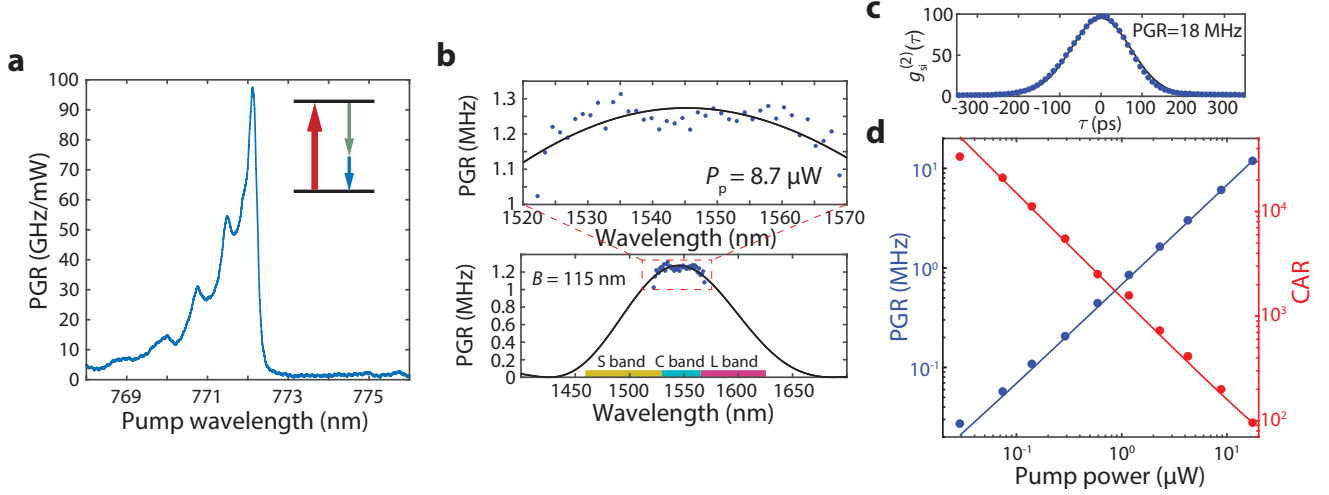


FIG. 3. **a.** Dependence of the total SPDC pair generation rate (PGR) efficiency on the pump wavelength. **b.** SPDC spectrum sampled by a DWDM with $P_p = 8.7 \mu\text{W}$. The solid line is a sinc^2 function fitting, yielding a bandwidth of 115 nm (14.4 THz). **c.** Measured $g_{\text{si}}^{(2)}(\tau)$ for PGR = 18 MHz in one DWDM channel. Solid line is Gaussian fitting. **d.** Pair generation rate in one DWDM channel and coincidence-to-accidental counts ratio (CAR) for various pump powers. Solid lines are linear fitting.

interference due to the bending of the multimode waveguide. The SHG nonlinear transfer function of the meander waveguide is given by $\left(\frac{\sin N(x+\phi)}{N \sin(x+\phi)} \frac{\sin x}{x}\right)^2$ (Methods), where $x = \frac{\Delta k L_0}{2}$, $\Delta k = 2k_\omega - k_{2\omega}$, L_0 is the length of the waveguide in one row, N is the number of rows, and 2ϕ is the total phase mismatch between the two modes in a 180° turn. For phase-matched fundamental- and second-harmonic modes in the straight waveguide, they become phase mismatched in the turn because of the change of the waveguide width and waveguide bending. A narrow waveguide section with a tunable length (Fig. 2b inset) is introduced to compensate the phase mismatch due to the bending waveguide such that the total phase mismatch 2ϕ through the 180° turn, including the tapering section, is multiple 2π . As a result, the transfer function can be recovered to the ideal sinc^2 function.

A tunable continuous-wave telecom band laser is employed for the measurement of second-harmonic generation. The output light from the waveguide passes through a 1550 nm/775 nm wavelength division multiplexer (WDM) to filter the residual pump before the second-harmonic intensity is measured. Fig. 2c shows the SHG intensity of a 1.6 mm long waveguide as the pump wavelength is swept, where a peak on-chip SH power $P_{\text{SHG}} = 80 \mu\text{W}$ is observed for the pump wavelength 1542.1 nm and an on-chip pump power $P_p = 1.56 \text{ mW}$. This corresponds to a normalized SHG efficiency of $128,000\%/W/\text{cm}^2$. In comparison, normalized SHG efficiency of $2,500\%/W/\text{cm}^2$ was achieved in lossy InGaP waveguides with phase-matched higher-order modes before [28]. A quadratic relationship between P_{SHG} and P_p is observed in the pump non-depleted region (Fig. 2d). Additionally, we explored the tunability of the

waveguide's phase-matching condition through temperature tuning of the device. In Fig. 2e, we present the measured SHG spectrum at several temperatures up to 95°C , constrained by the thermoelectric cooler element. A tuning range of 12.7 nm and a temperature-induced shift of $0.17 \text{ nm}/\text{C}$ in the phase-matching wavelength are measured.

The SHG efficiency realized in the InGaP nonlinear nanophotonic waveguide represents a substantial advance, in particular, in the crucial telecommunication band. Fig. 2f displays the normalized SHG efficiency and 1550 nm band loss of the best telecommunication C band waveguide SHG, to our knowledge, of several $\chi^{(2)}$ nonlinear photonics platforms (a more comprehensive list is provided in SI). The InGaP nanophotonic waveguide surpasses thin-film PPLN waveguides by nearly two orders of magnitude in terms of normalized nonlinear conversion efficiency [30, 31], while maintaining a low 1550 nm wavelength loss of $0.8 \pm 0.4 \text{ dB}/\text{cm}$, which is consistent with the measured Q_i of microring resonators. The nonlinear efficiency of $P_{\text{SHG}}/P_p^2 = 3280\%/W$ achieved in the 1.6 mm long InGaP waveguide is comparable to the centimeter-long PPLN waveguide made with the adapted poling technique recently [31]. For longer InGaP waveguides, we find the nonlinear efficiency deviates from the L^2 scaling because of the thickness nonuniformity of the thin film (SI). This can be mitigated using the adapted phase-matching technique [31], by varying the waveguide width according to the pre-calibrated InGaP film thickness to keep the phase-matching condition along the entire waveguide.

Utilizing the InGaP nonlinear nanophotonic waveguide, we demonstrate an ultra-bright, broadband time-energy entangled photon source via spontaneous para-

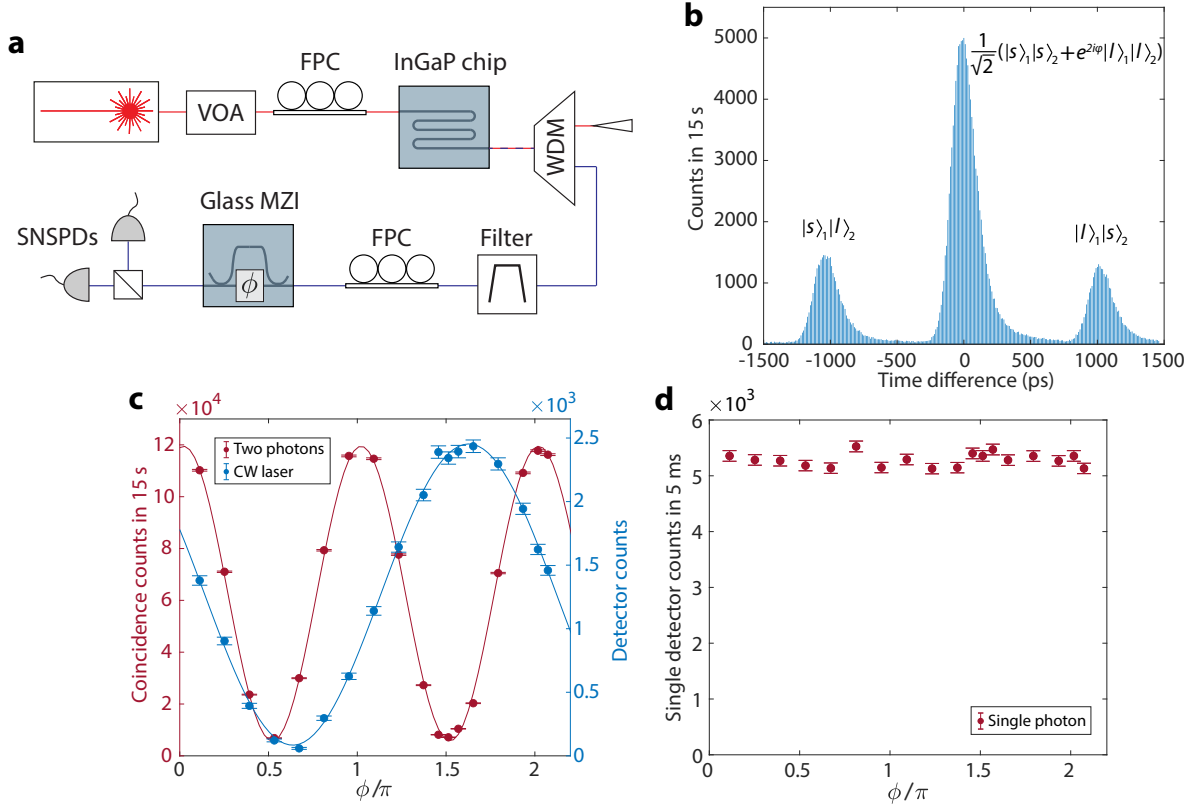


FIG. 4. **a**. Schematic of the measurement of the time-energy entanglement of the SPDC photons. VOA: variable optical attenuator. FPC: fiber polarization controller. **b**. Two-photon time difference histogram. The binwidth is 10 ps. The middle peak corresponds to the time-energy entangled state. **c**. Coincidence counts in 800 ps binwidth integrated in 15 s of the SPDC photon pair for various interferometer phases (red) and the interference fringe of a CW laser (blue). Solid lines are sinusoidal function fitting. Error bars represent the shot noise. **d**. Counts in 5 ms of SPDC photons in one SNSPD.

metric down-conversion (SPDC). For a phase-matched nonlinear waveguide, the internal efficiency of the pair generation via SPDC can be related to the SHG efficiency by [38]

$$\begin{aligned}
 P_{\text{SPDC}}/P_p &\approx \frac{\hbar\omega_p L^{3/2}}{3\sqrt{2\pi} |\text{GVD}(\frac{\omega_p}{2})|} \eta_{\text{SHG}} \\
 &= \frac{\hbar\omega_p L^2 \Delta f_{\text{FWHM}}}{3\sqrt{2\pi}\alpha} \eta_{\text{SHG}}, \quad (2)
 \end{aligned}$$

where $\text{GVD}(\frac{\omega_p}{2})$ is the group velocity dispersion at $\frac{\omega_p}{2}$, $\alpha = \frac{1}{\pi} \sqrt{2 \text{sinc}^{-1} \frac{1}{\sqrt{2}}}$, and Δf_{FWHM} is the bandwidth of the SPDC photons given by

$$\Delta f_{\text{FWHM}} = \frac{\alpha}{\sqrt{|\text{GVD}(\frac{\omega_p}{2})| L}}. \quad (3)$$

We pumped the phase-matched waveguide with a tunable 780 nm band continuous-wave laser to generate telecommunication band SPDC photons. After filtering the residual pump, the SPDC photons were measured

using either regular photodetectors or superconducting-nanowire single-photon detectors (SNSPDs). Fig. 3a shows the total photon pair generation rate efficiency via a 1.6 mm long waveguide measured with $P_p = 135 \mu\text{W}$. At the phase-matching wavelength of 772.12 nm, a peak pair generation rate of 97 GHz/mW, corresponding to an internal efficiency of 2.5×10^{-5} , is observed. To measure the bandwidth of the SPDC photons, we used a dense wavelength division-multiplexer (DWDM) with 40 channels and a 120 GHz channel bandwidth. The measured SPDC photon rate through each channel for $P_p = 8.7 \mu\text{W}$ is displayed in Fig. 3b (the fiber coupling is not optimized for this measurement). The data is fitted using a sinc^2 function and the SPDC photon bandwidth is inferred to be 14.4 THz (115 nm). The measured bandwidth agrees with the theoretical calculation using Eq. 3 (SI). This leads to a per-bandwidth pair generation rate of 6.7 GHz/mW/THz (840 MHz/mW/nm). In Table I, we compare the telecommunication C band SPDC photon pair generation in the InGaP waveguide and thin-film (TF) PPLN waveguides of several recent works. The InGaP waveguide SPDC source shows a rate efficiency at least an order of magnitude higher while retaining

a large bandwidth. We also noticed a recent work of high-efficiency telecommunication L band SPDC photon generation in AlGaAs waveguides [12]. A more comprehensive summary of broadband photon pair sources can be found, for example, in Ref. [39].

TABLE I. **Telecommunication C band SPDC photon pair generation in TF PPLN and InGaP waveguides**

Material	Rate (GHz/mW/THz)	Bandwidth (THz)	Waveguide length (mm)
TF PPLN [40]	0.12	–	10
TF PPLN [4]	0.46	–	5
TF PPLN [39]	0.13	100	5
InGaP (this work)	6.7	14.4	1.6

The second-order cross-correlation, $g_{\text{si}}^{(2)}(\tau)$, between the signal and idler photons via two DWDM channels was measured using a pair of SNSPDs. Fig. 3c displays the measured $g_{\text{si}}^{(2)}(\tau)$ for pair generation rate of 18 MHz in one DWDM channel. In the low gain regime, the zero-delay cross-correlation between the signal and idler is shown to be [41]

$$g_{\text{si}}^{(2)}(0) = 1 + \frac{4B}{R} \frac{\Gamma_s \Gamma_i}{(\Gamma_s + \Gamma_i)^2}, \quad (4)$$

where R and B are the total pair generation rate and bandwidth of the SPDC photons, respectively, and $\Gamma_{s,i}$ is the filter bandwidth of the signal and idler photons. For $\Gamma_s = \Gamma_i$, Eq. 4 indicates the inherent coincidence-to-accidental counts ratio (CAR) of the SPDC photon source is given by $\text{CAR} = g_{\text{si}}^{(2)}(0) - 1 = B/R$, i.e., the inverse of the photon pair rate per bandwidth. According to Eq. 2 ($B \equiv \Delta f_{\text{FWHM}}$ and $R \equiv P_{\text{SPDC}}/\hbar\omega_p$), $\text{CAR} \propto 1/(\eta_{\text{SHG}} L^2 P_p)$, which means for more efficient waveguides, same CAR can be achieved with less pump power. Due to the detector jitter (~ 100 ps), which is much larger than the coherence time of the SPDC photons filtered by a DWDM channel (120 GHz), the inherent $g_{\text{si}}^{(2)}(0)$ cannot be resolved and the measured CAR will be lower than the inherent value [41]. The measured CAR and pair generation rate in one DWDM channel for various pump power is shown in Fig. 3d (Methods). Nevertheless, $\text{CAR} > 10^4$ is observed for relatively low photon pair generation rate.

To demonstrate the time-energy entanglement of the SPDC photons, we measured the two-photon interference using an unbalanced Mach-Zehnder interferometer (MZI) [42], as illustrated in Fig. 4a (Methods). The unbalanced MZI is made from glass-based photonic integrated circuits with a path delay of $\tau_d = 1$ ns. The SPDC photons used in this measurement have a bandwidth of about 20 nm as they are filtered by a CWDM, leading to a single-photon coherence time much shorter than τ_d . The coherence time of the correlated signal-idler pair is determined by the continuous-wave pump laser, which is much longer than τ_d . As a result, the signal-idler photon pair can interfere through the unbalanced MZI while neither

can the signal or idler single photon. The signal-idler pair can travel through either the short (s) or long (l) path of the unbalanced MZI together, forming a time-energy entangled state $|\psi\rangle = \frac{1}{\sqrt{2}}(|s\rangle_1 |s\rangle_2 + e^{2i\phi} |l\rangle_1 |l\rangle_2)$, where ϕ is the phase difference between the two paths for light with a frequency that is half of the SPDC pump frequency. This entangled state can be post-selected, distinguishing itself from the other two states out of the interferometer, $|s\rangle_1 |l\rangle_2$ and $|l\rangle_1 |s\rangle_2$, using time-resolved coincidence detection (Methods).

Fig. 4b shows a measured time difference histogram of the SPDC photons. The coincidence counts around the zero delay, corresponding to the entangled state, depend on the interferometer phase as $\propto \frac{1}{2}(1 + \cos 2\phi)$. Fig. 4c shows the measured two-photon interference fringe by varying the temperature of the glass interferometer which changes ϕ . The two-photon fringe has a period of π while the fringe of a continuous-wave laser with a frequency about half of the pump frequency has a period of 2π . The counts of SPDC photons in one detector does not exhibit an interference fringe as expected (Fig. 4d). The measured two-photon interference visibility is 90.8%, which is limited by the imperfect glass photonic circuit MZI with the beam splitter ratio deviating from 50/50. The two-photon interference visibility is $\geq 98.6\%$ after correction for the interferometer imperfection (SI). The two-photon interference visibility exceeds the Clauser-Horne limit of $\frac{1}{\sqrt{2}} \approx 70.7\%$, which proves the photon pair entanglement [43].

Discussion

In summary, we have demonstrated a broadband second-order nonlinear photonics platform based on thin-film InGaP. With the optimized optical loss and phase-matching condition, the InGaP nanophotonic waveguide enables second-order nonlinear optical processes, including SHG and SPDC, with normalized efficiencies one to two orders of magnitude higher than the state of the art in the telecommunication C band. The nonlinear efficiency of the InGaP waveguides can be further enhanced using the adapted fabrication technique [31] to counter the thickness nonuniformity of thin films. The ultra-bright, broadband entangled photon pair source, covering the telecommunication C band, will be useful for high-rate wavelength-multiplexed entanglement distribution over long distances [44] and ultrafast spectroscopy using entangled photons [45]. Beyond that, the demonstrated InGaP nonlinear photonics platform is expected to enable unprecedented performances in applications ranging from squeezed light generation [46, 47] and optical parametric amplification [48] to few-photon quantum nonlinear optics [49], among others. Based on III-V semiconductors, the InGaP platform also enables monolithic integration of pump lasers [50] to realize electrically-injected nonlinear photonic sources.

Materials and methods

Device fabrication

The device fabrication follows Ref. [3]. The device pattern is defined using electron beam lithography

and transferred to InGaP layer via inductively coupled plasma reactive-ion etch (ICP-RIE) using a mixture of $\text{Cl}_2/\text{CH}_4/\text{Ar}$ gas. Then a layer of aluminum oxide is deposited via atomic layer deposition. The InGaP device is released from the GaAs substrate using citric acid-based selective etching.

Measurement

For the measurement of SPDC photons, we used a 780 nm band continuous-wave tunable diode laser as the pump. The light is polarization aligned by a fiber polarization controller, coupled into the device via a tapered fiber to generate the SPDC photons, and coupled back into the optical fiber using another tapered fiber. The residual pump is filtered by a 1550 nm/780 nm WDM. To measure the cross-correlation and CAR of the SPDC photons, the signal and idler photons are separated by a DWDM and detected using SNSPDs (Quantum Opus) and time-correlated single-photon counting module (Swabian). The coincidence and accidental counts are integrated in a time binwidth of 10 ps. To measure the time-energy entanglement of the SPDC photons, both signal and idler photons are filtered by the same CWDM channel and then pass through a glass waveguide unbalanced MZI (Teem Photonics). The two-photon coincidences are detected by two SNSPDs after the 50/50 beam splitter.

Nonlinear transfer function

The transfer function of SHG is calculated as

$$\mathcal{F}(L) = \left| \frac{1}{L} \int_0^L e^{i \int_0^z \Delta\phi dz'} dz \right|^2, \quad (5)$$

where $\Delta\phi$ is the phase mismatch between the fundamental- and second-harmonic modes. For a meander waveguide,

$$\begin{aligned} \mathcal{F}(L) &= \left| \frac{1}{L} \sum_n \int_{nL_0}^{(n+1)L_0} e^{i(\Delta kz + 2n\phi)} dz \right|^2 \\ &= \left| \frac{e^{i\Delta kL_0} - 1}{i\Delta kL} \frac{e^{iN(\Delta kL_0 + 2\phi)} - 1}{e^{i(\Delta kL_0 + 2\phi)} - 1} \right|^2 \\ &= \left(\frac{\sin(\Delta kL_0/2)}{\Delta kL/2} \frac{\sin(N(\Delta kL_0/2 + \phi))}{\sin(\Delta kL_0/2 + \phi)} \right)^2, \end{aligned} \quad (6)$$

where $\Delta k = 2k_\omega - k_{2\omega}$, L_0 is the length of the waveguide in one row, N is the number of rows, and 2ϕ is the total phase mismatch between the two modes for a 180° turn.

Acknowledgements

This work was supported by US National Science Foundation (Grant No. ECCS-2223192), NSF Quantum Leap Challenge Institute QLCI-HQAN (Grant No. 2016136), and U.S. Department of Energy Office of Science National Quantum Information Science Research Centers.

Author contributions

Y.Z., J.A., and A.K.M.N.H. performed the simulation. J.A. and Y.M. fabricated the device. J.A., Y.Z., Y.M., and A.K.M.N.H. measured the device and analyzed the data. J.A., Y.Z., and K.F. wrote the manuscript.

Conflict of interest

The authors declare no competing interests.

-
- [1] P.A. Franken, A.E. Hill, C.W. Peters, and G. Weinreich, "Generation of optical harmonics," *Physical Review Letters* **7**, 118 (1961).
- [2] Juanjuan Lu, Ming Li, Chang-Ling Zou, Ayed Al Sayem, and Hong X. Tang, "Toward 1% single-photon anharmonicity with periodically poled lithium niobate microring resonators," *Optica* **7**, 1654–1659 (2020).
- [3] Mengdi Zhao and Kejie Fang, "InGaP quantum nanophotonic integrated circuits with 1.5% nonlinearity-to-loss ratio," *Optica* **9**, 258–263 (2022).
- [4] Jie Zhao, Chaoxuan Ma, Michael Rüsing, and Shayan Mookherjee, "High quality entangled photon pair generation in periodically poled thin-film lithium niobate waveguides," *Physical Review Letters* **124**, 163603 (2020).
- [5] Henning Vahlbruch, Moritz Mehmet, Karsten Danzmann, and Roman Schnabel, "Detection of 15 dB squeezed states of light and their application for the absolute calibration of photoelectric quantum efficiency," *Physical Review Letters* **117**, 110801 (2016).
- [6] Luis Ledezma, Ryoto Sekine, Qiushi Guo, Rajveer Nehra, Saman Jahani, and Alireza Marandi, "Intense optical parametric amplification in dispersion-engineered nanophotonic lithium niobate waveguides," *Optica* **9**, 303–308 (2022).
- [7] Xiang Guo, Chang-Ling Zou, Hojoong Jung, and Hong X. Tang, "On-chip strong coupling and efficient frequency conversion between telecom and visible optical modes," *Physical Review Letters* **117**, 123902 (2016).
- [8] Kaustubh Vyas, Daniel H.G. Espinosa, Daniel Hutama, Shubhendra Kumar Jain, Rania Mahjoub, Ehsan Mobini, Kashif M. Awan, Jeff Lundeen, and Ksenia Dolgaleva, "Group III-V semiconductors as promising nonlinear integrated photonic platforms," *Advances in Physics: X* **7**, 2097020 (2022).
- [9] M. Ohashi, T. Kondo, R. Ito, S. Fukatsu, Y. Shiraki, K. Kumata, and S.S. Kano, "Determination of quadratic nonlinear optical coefficient of $\text{Al}_x\text{Ga}_{1-x}\text{As}$ system by the method of reflected second harmonics," *Journal of Applied Physics* **74**, 596–601 (1993).
- [10] C.P. Michael, K. Srinivasan, T.J. Johnson, O. Painter, K.H. Lee, K. Hennessy, H. Kim, and E. Hu, "Wavelength- and material-dependent absorption in GaAs and AlGaAs microcavities," *Applied Physics Letters* **90** (2007).
- [11] Liang Lin and John Robertson, "Passivation of interfacial defects at III-V oxide interfaces," *Journal of Vacuum Science & Technology B* **30** (2012).

- [12] Marlon Placke, Jan Schlegel, Felix Mann, Pietro Della Casa, Andreas Thies, Markus Weyers, Günther Tränkle, and Sven Ramelow, “Telecom-Band Spontaneous Parametric Down-Conversion in AlGaAs-on-Insulator Waveguides,” *Laser & Photonics Reviews*, 2301293 (2024).
- [13] N. Pan, J. Elliott, M. Knowles, D.P. Vu, K. Kishimoto, J.K. Twynam, H. Sato, M.T. Fresina, and G.E. Stillman, “High reliability InGaP/GaAs HBT,” *IEEE Electron Device Letters* **19**, 115–117 (1998).
- [14] Tatsuya Takamoto, Minoru Kaneiwa, Mitsuru Imaizumi, and Masafumi Yamaguchi, “InGaP/GaAs-based multi-junction solar cells,” *Progress in Photovoltaics: Research and Applications* **13**, 495–511 (2005).
- [15] J. Jiang, S. Tsao, T. O’sullivan, W. Zhang, H. Lim, T. Sills, K. Mi, M. Razeghi, G.J. Brown, and M.Z. Tidrow, “High detectivity InGaAs/InGaP quantum-dot infrared photodetectors grown by low pressure metalorganic chemical vapor deposition,” *Applied Physics Letters* **84**, 2166–2168 (2004).
- [16] C. Patrik T. Svensson, Thomas Märtensson, Johanna Trägårdh, Christina Larsson, Michael Rask, Dan Hessman, Lars Samuelson, and Jonas Ohlsson, “Monolithic GaAs/InGaP nanowire light emitting diodes on silicon,” *Nanotechnology* **19**, 305201 (2008).
- [17] V. Eckhouse, I. Cestier, G. Eisenstein, S. Combrié, P. Colman, A. De Rossi, M. Santagiustina, C.G. Smeda, and G. Vadalà, “Highly efficient four wave mixing in GaInP photonic crystal waveguides,” *Optics Letters* **35**, 1440–1442 (2010).
- [18] Pierre Colman, Chad Husko, Sylvain Combrié, Isabelle Sagnes, Chee Wei Wong, and Alfredo De Rossi, “Temporal solitons and pulse compression in photonic crystal waveguides,” *Nature Photonics* **4**, 862–868 (2010).
- [19] Utsav D. Dave, Charles Ciret, Simon-Pierre Gorza, Sylvain Combrie, Alfredo De Rossi, Fabrice Raineri, Gunther Roelkens, and Bart Kuyken, “Dispersive-wave-based octave-spanning supercontinuum generation in InGaP membrane waveguides on a silicon substrate,” *Optics Letters* **40**, 3584–3587 (2015).
- [20] Gabriel Marty, Sylvain Combrié, Fabrice Raineri, and Alfredo De Rossi, “Photonic crystal optical parametric oscillator,” *Nature Photonics* **15**, 53–58 (2021).
- [21] Alexandre Chopin, Andrea Barone, Inès Ghorbel, Sylvain Combrié, Daniele Bajoni, Fabrice Raineri, Matteo Galli, and Alfredo De Rossi, “Ultra-efficient generation of time-energy entangled photon pairs in an InGaP photonic crystal cavity,” *Communications Physics* **6**, 77 (2023).
- [22] W.H.P. Pernice, C. Xiong, C. Schuck, and H. X. Tang, “Second harmonic generation in phase matched aluminum nitride waveguides and micro-ring resonators,” *Applied Physics Letters* **100**, 223501 (2012).
- [23] Cheng Wang, Xiao Xiong, Nicolas Andrade, Vivek Venkataraman, Xi-Feng Ren, Guang-Can Guo, and Marko Lončar, “Second harmonic generation in nanostructured thin-film lithium niobate waveguides,” *Optics Express* **25**, 6963–6973 (2017).
- [24] Norman A. Sanford, A.V. Davydov, Denis V. Tsvetkov, A.V. Dmitriev, Stacia Keller, U.K. Mishra, Steven P. DenBaars, S.S. Park, J.Y. Han, and R.J. Molnar, “Measurement of second order susceptibilities of GaN and AlGaIn,” *Journal of Applied Physics* **97** (2005).
- [25] Hiroaki Sato, Makoto Abe, Ichiro Shoji, Jun Suda, and Takashi Kondo, “Accurate measurements of second-order nonlinear optical coefficients of 6H and 4H silicon carbide,” *JOSA B* **26**, 1892–1896 (2009).
- [26] Ichiro Shoji, Takashi Kondo, Ayako Kitamoto, Masayuki Shirane, and Ryoichi Ito, “Absolute scale of second-order nonlinear-optical coefficients,” *JOSA B* **14**, 2268–2294 (1997).
- [27] Yoshiyasu Ueno, Vincent Ricci, and George I. Stegeman, “Second-order susceptibility of Ga_{0.5}In_{0.5}P crystals at 1.5 μm and their feasibility for waveguide quasi-phase matching,” *JOSA B* **14**, 1428–1436 (1997).
- [28] Nicolas Poulvellarie, Carlos Mas Arabi, Charles Ciret, Sylvain Combrié, Alfredo De Rossi, Marc Haelterman, Fabrice Raineri, Bart Kuyken, Simon-Pierre Gorza, and François Leo, “Efficient type II second harmonic generation in an indium gallium phosphide on insulator wire waveguide aligned with a crystallographic axis,” *Optics Letters* **46**, 1490–1493 (2021).
- [29] Albert Peralta Amores and Marcin Swillo, “Low-Temperature Bonding of Nanolayered InGaP/SiO₂ Waveguides for Spontaneous-Parametric Down Conversion,” *ACS Applied Nano Materials* **5**, 2550–2557 (2022).
- [30] Cheng Wang, Carsten Langrock, Alireza Marandi, Marc Jankowski, Mian Zhang, Boris Desiatov, Martin M Fejer, and Marko Lončar, “Ultra-high-efficiency wavelength conversion in nanophotonic periodically poled lithium niobate waveguides,” *Optica* **5**, 1438–1441 (2018).
- [31] Pao-Kang Chen, Ian Briggs, Chaohan Cui, Liang Zhang, Manav Shah, and Linran Fan, “Adapted poling to break the nonlinear efficiency limit in nanophotonic lithium niobate waveguides,” *Nature Nanotechnology* **19**, 44–50 (2024).
- [32] Stuart May, Michael Kues, Matteo Clerici, and Marc Sorel, “Second-harmonic generation in AlGaAs-on-insulator waveguides,” *Optics Letters* **44**, 1339–1342 (2019).
- [33] Konstantinos Pantzas, Sylvain Combrié, Myriam Bailly, Raphaël Mandouze, Francesco Rinaldo Talenti, Abdelmounaim Harouri, Bruno Gérard, Grégoire Beaudoin, Luc Le Gratiet, Gilles Patriarche, *et al.*, “Continuous-wave second-harmonic generation in orientation-patterned gallium phosphide waveguides at telecom wavelengths,” *ACS Photonics* **9**, 2032–2039 (2022).
- [34] Yi Zheng, Ailun Yi, Chaochao Ye, Kresten Yvind, Han Zhang, Xin Ou, and Minhao Pu, “Efficient second-harmonic generation in silicon carbide nanowaveguides,” in *2022 Conference on Lasers and Electro-Optics (CLEO)* (IEEE, 2022) pp. 1–2.
- [35] Utsav D. Dave, Bart Kuyken, François Leo, Simon-Pierre Gorza, Sylvain Combrie, Alfredo De Rossi, Fabrice Raineri, and Gunther Roelkens, “Nonlinear properties of dispersion engineered InGaP photonic wire waveguides in the telecommunication wavelength range,” *Optics Express* **23**, 4650–4657 (2015).
- [36] Biswarup Guha, Felix Marsault, Fabian Cadiz, Laurence Morgenroth, Vladimir Ulin, Vladimir Berkovitz, Aristide Lemaître, Carmen Gomez, Alberto Amo, Sylvain Combrié, *et al.*, “Surface-enhanced gallium arsenide photonic resonator with quality factor of 6×10^6 ,” *Optica* **4**, 218–221 (2017).
- [37] Rui Luo, Yang He, Hanxiao Liang, Mingxiao Li, and Qiang Lin, “Highly tunable efficient second-harmonic generation in a lithium niobate nanophotonic waveguide,”

- uide,” *Optica* **5**, 1006–1011 (2018).
- [38] Ramesh Kumar and Joyee Ghosh, “Parametric down-conversion in ppLN ridge waveguide: a quantum analysis for efficient twin photons generation at 1550 nm,” *Journal of Optics* **20**, 075202 (2018).
- [39] Usman A. Javid, Jingwei Ling, Jeremy Staffa, Mingxiao Li, Yang He, and Qiang Lin, “Ultrabroadband entangled photons on a nanophotonic chip,” *Physical Review Letters* **127**, 183601 (2021).
- [40] H. Jin, F.M. Liu, P. Xu, J.L. Xia, M.L. Zhong, Y. Yuan, J.W. Zhou, Y.X. Gong, W. Wang, and S.N. Zhu, “On-chip generation and manipulation of entangled photons based on reconfigurable lithium-niobate waveguide circuits,” *Physical Review Letters* **113**, 103601 (2014).
- [41] Christoph Clausen, Félix Bussières, Alexey Tiranov, Harald Herrmann, Christine Silberhorn, Wolfgang Sohler, Mikael Afzelius, and Nicolas Gisin, “A source of polarization-entangled photon pairs interfacing quantum memories with telecom photons,” *New Journal of Physics* **16**, 093058 (2014).
- [42] J. Brendel, E. Mohler, and W. Martienssen, “Time-resolved dual-beam two-photon interferences with high visibility,” *Physical Review Letters* **66**, 1142 (1991).
- [43] John F. Clauser and Michael A. Horne, “Experimental consequences of objective local theories,” *Physical Review D* **10**, 526 (1974).
- [44] Sören Wengerowsky, Siddarth Koduru Joshi, Fabian Steinlechner, Hannes Hübel, and Rupert Ursin, “An entanglement-based wavelength-multiplexed quantum communication network,” *Nature* **564**, 225–228 (2018).
- [45] Zhedong Zhang, Tao Peng, Xiaoyu Nie, Girish S. Agarwal, and Marlan O. Scully, “Entangled photons enabled time-frequency-resolved coherent Raman spectroscopy and applications to electronic coherences at femtosecond scale,” *Light: Science & Applications* **11**, 274 (2022).
- [46] Rajveer Nehra, Ryoto Sekine, Luis Ledezma, Qiushi Guo, Robert M Gray, Arkadev Roy, and Alireza Marandi, “Few-cycle vacuum squeezing in nanophotonics,” *Science* **377**, 1333–1337 (2022).
- [47] Hubert S. Stokowski, Timothy P. McKenna, Taewon Park, Alexander Y. Hwang, Devin J. Dean, Oguz Tolga Celik, Vahid Ansari, Martin M. Fejer, and Amir H. Safavi-Naeini, “Integrated quantum optical phase sensor in thin film lithium niobate,” *Nature Communications* **14**, 3355 (2023).
- [48] Johann Riemensberger, Nikolai Kuznetsov, Junqiu Liu, Jijun He, Rui Ning Wang, and Tobias J. Kippenberg, “A photonic integrated continuous-travelling-wave parametric amplifier,” *Nature* **612**, 56–61 (2022).
- [49] Ryotatsu Yanagimoto, Edwin Ng, Marc Jankowski, Hideo Mabuchi, and Ryan Hamerly, “Temporal trapping: a route to strong coupling and deterministic optical quantum computation,” *Optica* **9**, 1289–1296 (2022).
- [50] M.A. Majid, A.A. Al-Jabr, H.M. Oubei, M.S. Alias, D.H. Anjum, T.K. Ng, and B.S. Ooi, “First demonstration of InGaP/InAlGaP based orange laser emitting at 608 nm,” *Electronics Letters* **51**, 1102–1104 (2015).

Supplementary Information for: “InGaP $\chi^{(2)}$ integrated photonics platform for broadband, ultra-efficient nonlinear conversion and entangled photon generation”

Joshua Akin,^{1,2,*} Yunlei Zhao,^{1,2,*} Yuvraj Misra,^{1,2} A. K. M. Naziul Haque,^{1,2} and Kejie Fang^{1,2,†}

¹*Holonyak Micro and Nanotechnology Laboratory and Department of Electrical and Computer Engineering, University of Illinois at Urbana-Champaign, Urbana, IL 61801 USA*

²*Illinois Quantum Information Science and Technology Center, University of Illinois at Urbana-Champaign, Urbana, IL 61801 USA*

I. MICRORING QUALITY FACTOR

Microring resonators of different radius are made and the quality factor of the 1550 nm band TE₀₀ resonances are measured. The result is displayed in Fig. S1. The intrinsic quality factor of the microring resonator is found to be bounded around 8×10^5 , which is limited by the absorption loss. The intrinsic quality factor can be decomposed as $1/Q_i = 1/Q_r + 1/Q_s + 1/Q_a$, where $1/Q_r$ is the radiation loss due to the curvature, $1/Q_s$ is the surface roughness caused scattering loss, $1/Q_a$ is the absorption loss. From numerical simulation, the radiation loss of microrings with radius larger than 5 μm is negligible. Below we calculate the scattering loss using the model of Ref. [1] for the microring resonators.

The splitting of the microring resonances due to surface roughness induced backscattering is given by

$$\frac{\Delta\lambda}{\lambda} = 2\sqrt{2}\pi^{3/4}\xi\frac{V_s}{V_r}, \quad (\text{S1})$$

where V_r is the physical volume of the microring, V_s is the effective volume of a typical scatterer, and ξ is the relative dielectric contrast constant defined as

$$\xi = \frac{\bar{n}^2(n_r^2 - n_0^2)}{n_r^2(\bar{n}^2 - n_0^2)}. \quad (\text{S2})$$

n_r , n_0 , and \bar{n} are the indices of refraction for the InGaP microring, surrounding medium, and 2D effective slab, respectively.

The surface roughness induced scattering loss Q_s is given by

$$Q_s = \frac{3\lambda^3}{16\pi^{7/2}n_0(n_r^2 - n_0^2)\xi V_s^2}. \quad (\text{S3})$$

From Eqs. S1 and S3, we can calculate Q_s using the measured resonance splitting $\Delta\lambda$. Q_s is found to be on the order of 10^9 , as shown in Fig. S1, which is much larger than the measured Q_i . As a result, we conclude Q_i is limited by the material absorption loss.

II. SECOND HARMONIC GENERATION EFFICIENCY

For an InGaP waveguide with phase-matched fundamental-harmonic (FH) mode a and second-harmonic (SH) mode b , the SHG efficiency can be calculated using [2]:

$$\eta_{\text{SHG}} = \frac{\omega_a^2}{2n_a^2n_b\epsilon_0c^3} \left(\frac{\int d\mathbf{r}\chi_{xyz}^{(2)} \sum_{i \neq j \neq k} E_{bi}^* E_{aj} E_{ak}}{\int d\mathbf{r}|\mathbf{E}_a|^2 \sqrt{\int d\mathbf{r}|\mathbf{E}_b|^2}} \right)^2, \quad (\text{S4})$$

* These authors contributed equally to this work.

† kfang3@illinois.edu

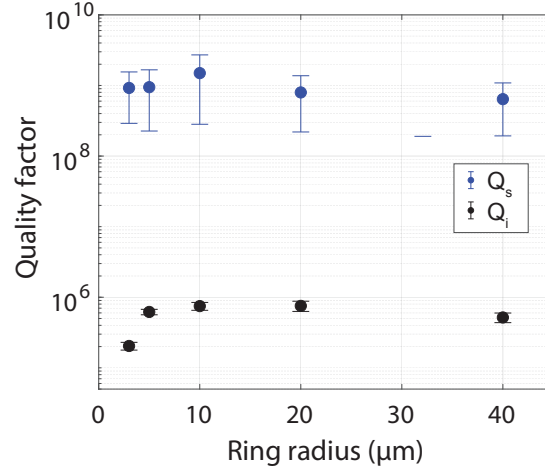


FIG. S1. Quality factor of the 1550 nm band TE₀₀ resonances of microring resonators of different radius.

with the normalization integrals only considering the transverse field components. Because the second-order susceptibility of InGaP only has the term $\chi_{xyz}^{(2)}$, the FH and SH modes are chosen to be TE₀₀ and TM₀₀, respectively. Consider the orientation of the waveguide has an angle of θ with respect to the (100) direction of InGaP. We denote the electric field in the waveguide frame as $(E_{x'}, E_{y'}, E_{z'})$, where the $x' - z'$ plane is the waveguide cross-section plane and y' direction is along the waveguide. The electric field in the crystal frame is denoted as (E_x, E_y, E_z) . As a result, $E_x = E_{x'} \cos \theta + E_{y'} \sin \theta$, $E_y = E_{x'} \sin \theta - E_{y'} \cos \theta$, and $E_z = E_{z'}$. Because the FH and SH modes are TE₀₀ and TM₀₀, respectively, the dominant contribution to the numerator integral of Eq. S4 is given by

$$\begin{aligned}
& \int d\mathbf{r} \chi_{xyz}^{(2)} \sum_{i \neq j \neq k} E_{bi}^* E_{aj} E_{ak} \\
&= 2 \int d\mathbf{r} \chi_{xyz}^{(2)} E_{bz}^* E_{ax} E_{ay} \\
&= 2 \int d\mathbf{r} \chi_{xyz}^{(2)} E_{bz'}^* (E_{ax'} \cos \theta + E_{ay'} \sin \theta) (E_{ax'} \sin \theta - E_{ay'} \cos \theta) \\
&= \int d\mathbf{r} \chi_{xyz}^{(2)} E_{bz'}^* (E_{ax'}^2 - E_{ay'}^2) \sin 2\theta - 2 \int d\mathbf{r} \chi_{xyz}^{(2)} E_{bz'}^* E_{ax'} E_{ay'} \cos 2\theta \\
&= \int d\mathbf{r} \chi_{xyz}^{(2)} E_{bz'}^* (E_{ax'}^2 - E_{ay'}^2) \sin 2\theta.
\end{aligned} \tag{S5}$$

The second term in the second-last line is zero because $E_{ay'}$ is odd while $E_{ax'}$ and $E_{bz'}$ are even. Other terms contributing to the nonlinear interaction include

$$\begin{aligned}
& 2 \int d\mathbf{r} \chi_{xyz}^{(2)} E_{az} (E_{bx}^* E_{ay} + E_{by}^* E_{ax}) \\
&= 2 \int d\mathbf{r} \chi_{xyz}^{(2)} E_{az'} (E_{bx'}^* \cos \theta + E_{by'}^* \sin \theta) (E_{ax'} \sin \theta - E_{ay'} \cos \theta) \\
&\quad + 2 \int d\mathbf{r} \chi_{xyz}^{(2)} E_{az'} (E_{bx'}^* \sin \theta - E_{by'}^* \cos \theta) (E_{ax'} \cos \theta + E_{ay'} \sin \theta) \\
&= 2 \int d\mathbf{r} \chi_{xyz}^{(2)} E_{az'} (E_{bx'}^* E_{ax'} \sin 2\theta - E_{bx'}^* E_{ay'} \cos 2\theta - E_{by'}^* E_{ax'} \cos 2\theta - E_{by'}^* E_{ay'} \sin 2\theta) \\
&= 0,
\end{aligned} \tag{S6}$$

which vanish because of the symmetry of the modes.

As a result, the mode overlap integral is maximized when $\theta = \frac{\pi}{4}$. The optimized SHG efficiency thus is given by

$$\eta_{\text{SHG}} = \frac{\omega_a^2}{2n_a^2 n_b \epsilon_0 c^3} \left(\frac{\int d\mathbf{r} \chi_{xyz}^{(2)} E_{bz'}^* (E_{ax'}^2 - E_{ay'}^2)}{\int d\mathbf{r} |\mathbf{E}_a|^2 \sqrt{\int d\mathbf{r} |\mathbf{E}_b|^2}} \right)^2. \quad (\text{S7})$$

The E field of the FH and SH modes are obtained by finite element simulation and the optimized SHG efficiency for 110 nm thick InGaP phase-matched waveguide and 1550 nm FH wavelength is found to be $\eta_{\text{SHG}} = 130,000\%/W/\text{cm}^2$, which agrees with the measured value.

III. NONLINEAR EFFICIENCY OF INGAP WAVEGUIDES

The nonlinear efficiency of long InGaP waveguides is limited by the thickness nonuniformity of the thin film. Fig. S2a-c display the SHG spectrum of three waveguides with length 0.8, 1.6, and 3.2 mm, respectively, measured with $P_p = 1.56$ mW. It is observed that the spectrum of the 3.2 mm long waveguide distorts more due to the thickness nonuniformity as well as the phase mismatch at the 180° waveguide turn. Fig. S2d shows the peak nonlinear efficiency of the three waveguides. The nonlinear efficiency of the 3.2 mm long waveguide deviates from the L^2 scaling.

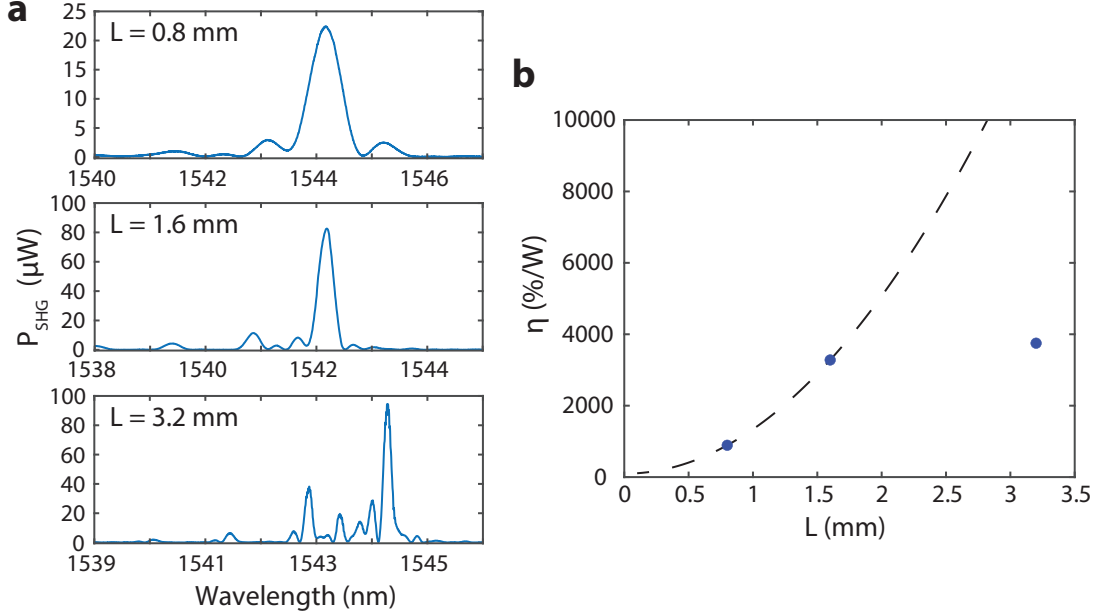


FIG. S2. **a-c.** Measured SHG spectrum of three waveguides with length 0.8, 1.6, and 3.2 mm, respectively. **d.** Peak nonlinear efficiency v. waveguide length. Dashed line indicates the L^2 scaling.

IV. BANDWIDTH OF WAVEGUIDE SPDC PHOTONS

The SPDC signal power in a bandwidth of $d\omega_s$ is given by [3]

$$dP_s = \frac{\hbar d_{\text{eff}}^2 P_p \omega_s^2 \omega_i L^2}{\pi \epsilon_0 c^3 n_s n_i n_p A_{\text{eff}}} \text{sinc}^2 \left(\frac{\Delta k L}{2} \right) d\omega_s, \quad (\text{S8})$$

where the d_{eff} is the nonlinear coefficient, L is the waveguide length, P_p is the pump power, A_{eff} is the effective interaction area, and Δk is the phase mismatch between the pump, signal and idler defined as

$$\Delta k = \frac{(n_p \omega_p - n_s \omega_s - n_i \omega_i)}{c}. \quad (\text{S9})$$

Eq. S8 shows the ideal sinc² function of the SPDC spectrum and the bandwidth of the SPDC photons can be calculated from Eq. S9.

The InGaP waveguide is designed to be perfectly phase matched for the degenerate signal and idler. Thus the nondegenerate signal and idler frequencies are expressed most conveniently as

$$\omega_{s,i} = \frac{\omega_p}{2} \pm \Delta\omega. \quad (\text{S10})$$

Using Eq. S9, the phase mismatch can be expressed in terms of the group velocity dispersion:

$$\Delta k = \text{GVD} \left(\frac{\omega_p}{2} \right) \Delta\omega^2, \quad (\text{S11})$$

where the group velocity dispersion is defined as

$$\text{GVD}(\omega_0) \equiv \frac{2}{c} \left(\frac{\partial n}{\partial \omega} \right)_{\omega=\omega_0} + \frac{\omega_0}{c} \left(\frac{\partial^2 n}{\partial \omega^2} \right)_{\omega=\omega_0}. \quad (\text{S12})$$

$n(\omega)$ is the effective mode index of the waveguide mode corresponding to the signal and idler. Using Eqs. S8 and S11, the full-width-half-maximum (FWHM) bandwidth of the SPDC spectrum is then given by

$$\Delta f_{\text{FWHM}} = \frac{\alpha}{\sqrt{|\text{GVD}(\frac{\omega_p}{2})|L}}, \quad (\text{S13})$$

where $\alpha = \frac{1}{\pi} \sqrt{2 \text{sinc}^{-1} \frac{1}{\sqrt{2}}}$.

For the waveguide used for the SPDC process, $L = 1.6$ mm and the pump frequency is $\omega_p/2\pi = 388.55$ THz. We simulated the dispersion of the effective mode index of the TE₀₀ waveguide mode around $\omega_p/2$ and found $|\text{GVD}(\frac{\omega_p}{2})| = 0.373$ (ps)²/m. This yields a SPDC bandwidth of 12.1 THz, which is close to the measured value.

V. TWO-PHOTON INTERFERENCE VISIBILITY

Consider an unbalanced Mach-Zehnder interferometer (MZI) consisting of two beam splitters, with transmission and reflection coefficients $T_{1(2)}$ and $R_{1(2)}$, which satisfy $T_k^2 + R_k^2 = 1$. For a single-photon input state, the output state of the MZI is given by

$$|1\rangle \rightarrow T_1 T_2 |s\rangle + R_1 R_2 e^{i\phi} |l\rangle, \quad (\text{S14})$$

where $|s\rangle$ and $|l\rangle$ represent the state in the short and long arm of the unbalanced MZI, respectively, and ϕ is the phase difference of the two arms. The visibility of the single-photon interference fringe thus is

$$V_1 = \frac{2T_1 T_2 R_1 R_2}{T_1^2 T_2^2 + R_1^2 R_2^2}. \quad (\text{S15})$$

The single-photon interference visibility can be characterized using a CW laser.

For a correlated two-photon input state $|1\rangle_1 |1\rangle_2$ generated via SPDC, without parasitic noises, the output state thus is given by

$$|1\rangle_1 |1\rangle_2 \rightarrow T_1^2 T_2^2 |s\rangle_1 |s\rangle_2 + T_1 T_2 R_1 R_2 e^{i\phi} |s\rangle_1 |l\rangle_2 + T_1 T_2 R_1 R_2 e^{i\phi} |l\rangle_1 |s\rangle_2 + R_1^2 R_2^2 e^{2i\phi} |l\rangle_1 |l\rangle_2, \quad (\text{S16})$$

where ϕ is the interferometer phase difference corresponding to half of the SPDC pump frequency. In this output state, only the first and last terms contribute to the two-photon interference, since they cannot be distinguished in

the two-photon coincidence measurement. The visibility of the two-photon interference is given by

$$V_2 = \frac{2T_1^2 T_2^2 R_1^2 R_2^2}{T_1^4 T_2^4 + R_1^4 R_2^4}. \quad (\text{S17})$$

Using Eqs. S15 and S17, the two interference visibilities are related by

$$V_2 = \frac{2}{\frac{4}{V_1^2} - 2}. \quad (\text{S18})$$

We model the measured two-photon interference visibility $V_{2,m}$ deviating from the ideal case (Eq. S18) using some uncorrelated counts x . We stress this is an effective model and it could represent other physical imperfection in the setup. The minimum and maximum two-photon coincidence counts are given by $C_{\min} = (T_1^2 T_2^2 - R_1^2 R_2^2)^2 + x$ and $C_{\max} = (T_1^2 T_2^2 + R_1^2 R_2^2)^2 + x$. The measured two-photon interference visibility thus is

$$V_{2,m} = \frac{2T_1^2 T_2^2 R_1^2 R_2^2}{T_1^4 T_2^4 + R_1^4 R_2^4 + x}. \quad (\text{S19})$$

Using Eqs. S15 and S19, we can find the bound of x :

$$\begin{aligned} x &= \frac{2}{V_{2,m}} T_1^2 T_2^2 R_1^2 R_2^2 - T_1^4 T_2^4 - R_1^4 R_2^4 \\ &= T_1^2 T_2^2 R_1^2 R_2^2 \left(\frac{2}{V_{2,m}} - \frac{4}{V_1^2} + 2 \right) \\ &= \mu^2 \left(\frac{(1 - R_1^2) R_1^2}{(\mu^2 - 1) R_1^2 + 1} \right)^2 \left(\frac{2}{V_{2,m}} - \frac{4}{V_1^2} + 2 \right) \\ &\leq \frac{\mu^2}{(\mu + 1)^4} \left(\frac{2}{V_{2,m}} - \frac{4}{V_1^2} + 2 \right) \\ &= x_{\max}, \end{aligned} \quad (\text{S20})$$

where $\mu = (1 + \sqrt{1 - V_1^2})/V_1$. In our experiment, the measured CW interference visibility and two-photon interference visibility are $V_1 = 97.9\%$ and $V_{2,m} = 90.8\%$, respectively, from which we find $x_{\max} = 0.00179$.

We can then estimate the inherent two-photon interference visibility, $V_{2,i}$, if we were to use a perfect unbalanced MZI with $T_k^2 = R_k^2 = \frac{1}{2}$,

$$V_{2,i} = \frac{\frac{1}{8}}{\frac{1}{8} + x} \geq \frac{\frac{1}{8}}{\frac{1}{8} + x_{\max}} = 98.6\%. \quad (\text{S21})$$

If we were to use a practically better interferometer with $V_1 = 99.8\%$ (achieved with $T_k^2 = 0.484$ and $R_k^2 = 0.516$), then using Eq. S19 and the estimated bound x_{\max} , the measured two-photon interference visibility will be $V_{2,m} \geq 97.8\%$.

VI. WAVEGUIDE SHG IN THIN-FILM $\chi^{(2)}$ PHOTONICS PLATFORMS

In Table S1, we summarize results, to our knowledge, of thin-film waveguide SHG in the telecommunication and near-infrared wavelength bands from recent works. The top half of the table before the break is in the telecommunication C band.

TABLE S1. Thin-film waveguide SHG performances

Material	$\chi^{(2)}$ (pm/V)	poling	pump wavelength (nm)	η_{SHG} ($\text{W}^{-1}\text{cm}^{-2}$)	η (W^{-1})	FH loss (dB/cm)
InGaP (this work)	$\chi_{xyz}^{(2)} = 220$	no	1550	128000%	3280%	0.8
InGaP [4]	$\chi_{xyz}^{(2)} = 220$	no	1536	2500%	12%	12
PGLN [5]	$\chi_{zzz}^{(2)} = 54$	no	1550	60%	31%	3
LN [2]	$\chi_{zzz}^{(2)} = 8.6$	no	1540	22%	5%	0.5
PPLN [6]	$\chi_{zzz}^{(2)} = 54$	yes	1550	2600%	42%	~ 1
PPLN [7]	$\chi_{zzz}^{(2)} = 54$	yes	1544	1000%	660%	0.7
PPLN [8]	$\chi_{zzz}^{(2)} = 54$	yes	1530	2000%	9000%	0.8
$\text{Al}_{0.27}\text{Ga}_{0.73}\text{As}$ [9]	$\chi_{xyz}^{(2)} = 210$	no	1560	1202%	87%	14
$\text{Al}_{0.19}\text{Ga}_{0.81}\text{As}$ [10]	$\chi_{xyz}^{(2)} = 220$	no	1590	1600%	16%	15
$\text{Al}_{0.2}\text{Ga}_{0.8}\text{As}$ [11]	$\chi_{xyz}^{(2)} = 210$	no	1580	23000%	477%	≤ 2
GaP [12]	$\chi_{yxx}^{(2)} = 70$	yes	1595	200%	14%	8
SiC [13]	$\chi_{zzz}^{(2)} = 25$	no	1584	60%	5%	0.4 [14]
GaAs [15]	$\chi_{xyz}^{(2)} = 240$	no	2025	13000%	250%	2
GaAs [16]	$\chi_{xyz}^{(2)} = 240$	no	1968	47600%	4000%	1.5

-
- [1] Matthew Borselli, Thomas J. Johnson, and Oskar Painter, “Beyond the Rayleigh scattering limit in high-Q silicon microdisks: theory and experiment,” *Optics Express* **13**, 1515–1530 (2005).
- [2] Rui Luo, Yang He, Hanxiao Liang, Mingxiao Li, and Qiang Lin, “Highly tunable efficient second-harmonic generation in a lithium niobate nanophotonic waveguide,” *Optica* **5**, 1006–1011 (2018).
- [3] Ramesh Kumar and Joyee Ghosh, “Parametric down-conversion in ppLN ridge waveguide: a quantum analysis for efficient twin photons generation at 1550 nm,” *Journal of Optics* **20**, 075202 (2018).
- [4] Nicolas Poulvellarie, Carlos Mas Arabi, Charles Ciret, Sylvain Combrié, Alfredo De Rossi, Marc Haelterman, Fabrice Raineri, Bart Kuyken, Simon-Pierre Gorza, and François Leo, “Efficient type II second harmonic generation in an indium gallium phosphide on insulator wire waveguide aligned with a crystallographic axis,” *Optics Letters* **46**, 1490–1493 (2021).
- [5] Cheng Wang, Xiao Xiong, Nicolas Andrade, Vivek Venkataraman, Xi-Feng Ren, Guang-Can Guo, and Marko Lončar, “Second harmonic generation in nano-structured thin-film lithium niobate waveguides,” *Optics Express* **25**, 6963–6973 (2017).
- [6] Cheng Wang, Carsten Langrock, Alireza Marandi, Marc Jankowski, Mian Zhang, Boris Desiatov, Martin M. Fejer, and Marko Lončar, “Ultrahigh-efficiency wavelength conversion in nanophotonic periodically poled lithium niobate waveguides,” *Optica* **5**, 1438–1441 (2018).
- [7] Hubert S. Stokowski, Timothy P. McKenna, Taewon Park, Alexander Y. Hwang, Devin J. Dean, Oguz Tolga Celik, Vahid Ansari, Martin M. Fejer, and Amir H. Safavi-Naeini, “Integrated quantum optical phase sensor in thin film lithium niobate,” *Nature Communications* **14**, 3355 (2023).
- [8] Pao-Kang Chen, Ian Briggs, Chaohan Cui, Liang Zhang, Manav Shah, and Linran Fan, “Adapted poling to break the nonlinear efficiency limit in nanophotonic lithium niobate waveguides,” *Nature Nanotechnology* **19**, 44–50 (2024).
- [9] Stuart May, Michael Kues, Matteo Clerici, and Marc Sorel, “Second-harmonic generation in AlGaAs-on-insulator waveguides,” *Optics Letters* **44**, 1339–1342 (2019).
- [10] Iannis Roland, Marco Ravaro, Stéphan Suffit, Pascal Filloux, Aristide Lemaître, Ivan Favero, and Giuseppe Leo, “Second-harmonic generation in suspended AlGaAs waveguides: A comparative study,” *Micromachines* **11**, 229 (2020).
- [11] Marlon Placke, Jan Schlegel, Felix Mann, Pietro Della Casa, Andreas Thies, Markus Weyers, Günther Tränkle, and Sven Ramelow, “Telecom-Band Spontaneous Parametric Down-Conversion in AlGaAs-on-Insulator Waveguides,” *Laser & Photonics Reviews*, 2301293 (2024).
- [12] Konstantinos Pantzas, Sylvain Combrié, Myriam Bailly, Raphaël Mandouze, Francesco Rinaldo Talenti, Abdelmounaim Harouri, Bruno Gérard, Grégoire Beaudoin, Luc Le Gratiet, Gilles Patriarche, *et al.*, “Continuous-wave second-harmonic generation in orientation-patterned gallium phosphide waveguides at telecom wavelengths,” *ACS Photonics* **9**, 2032–2039 (2022).
- [13] Yi Zheng, Ailun Yi, Chaochao Ye, Kresten Yvind, Han Zhang, Xin Ou, and Minhao Pu, “Efficient second-harmonic generation in silicon carbide nanowaveguides,” in *2022 Conference on Lasers and Electro-Optics (CLEO) (IEEE, 2022)* pp. 1–2.
- [14] Haiyan Ou, Xiaodong Shi, Yaoqin Lu, Manuel Kollmuss, Johannes Steiner, Vincent Tabouret, Mikael Syväjärvi, Peter Wellmann, and Didier Chaussende, “Novel Photonic Applications of Silicon Carbide,” *Materials* **16**, 1014 (2023).
- [15] Lin Chang, Andreas Boes, Xiaowen Guo, Daryl T. Spencer, M.J. Kennedy, Jon D. Peters, Nicolas Volet, Jeff Chiles, Abijith Kowligy, Nima Nader, *et al.*, “Heterogeneously integrated GaAs waveguides on insulator for efficient frequency conversion,” *Laser & Photonics Reviews* **12**, 1800149 (2018).

- [16] Eric J. Stanton, Jeff Chiles, Nima Nader, Galan Moody, Nicolas Volet, Lin Chang, John E. Bowers, Sae Woo Nam, and Richard P. Mirin, “Efficient second harmonic generation in nanophotonic GaAs-on-insulator waveguides,” *Optics Express* **28**, 9521–9532 (2020).